Research Article

Synthesis and Characterizations of CH₃NH₃PbI₃ : ZnS Microrods for Optoelectronic Applications

Mohammad Tanvir Ahmed,[1] Shariful Islam ⦿,[1] Muhammad Shahriar Bashar,[2] Md. Abul Hossain,[1] and Farid Ahmed[1]

[1]*Department of Physics, Jahangirnagar University, Dhaka 1342, Bangladesh*
[2]*IFRD Bangladesh Council of Scientific and Industrial Research, Dhanmondi, Dhaka 1205, Bangladesh*

Correspondence should be addressed to Shariful Islam; s_islam@juniv.edu

Organometallic perovskite is one of the potential materials in the various optoelectronic research fields. This study demonstrates the synthesis of CH₃NH₃PbI₃ : ZnS microrods via one-step spin coating for optoelectronic applications. Incorporation of ZnS in the perovskite material caused bandgap variation in the visible wavelength range. Structural and chemical properties have been observed using X-ray diffraction, scanning electron microscope, and Fourier transform infrared spectroscopy. The optical and electrical properties were studied via UV-Vis spectroscopy and impedance analyzer. The addition of ZnS caused to increase the optical absorption coefficient from $\sim 10^4 \, \text{cm}^{-1}$ to $\sim 10^5 \, \text{cm}^{-1}$. The bandgaps of the thin films were calculated using the Tauc relation and electrical method, obtained in the range 1.51 eV–1.64 eV, suitable for various optoelectronic applications.

1. Introduction

Organometallic perovskites (OMPs) are very multifunctional materials with widespread applications such as photodetectors, solar cells (SCs), field-effect transistors (FET), light-emitting diode, laser, light-emitting electrochemical cells, and so on [1]. They can offer a tunable bandgap and a better visible light absorption property, making them highly potential material for various optoelectronic (OE) applications. These plentiful applications led scientists all over the world to study the different properties of these materials. The material has also become very popular because of the easy synthesis process and low cost. The general formula of OMPs is ABX₃, where A, B, and *X* are monovalent organic cations (e.g., methylammonium and formamidinium), divalent metal cation (e.g., Pb²⁺ and Sn²⁺), and halogen anion, respectively [2]. One of the greatest successes of OMPs in SC technology is an efficient light absorber with a maximum conversion efficiency of 25.5%, which is reported by the national renewable energy laboratory [3].

The optical and electrical performances of a material highly depend on its crystal structure and bandgap. Depending on various crystal growth conditions, a material can offer different crystal structures (one-, two-, or three-dimensional). In the case of micro/nanorod structure, the bandgap also depends on the diameters. Hence, changing the diameters can cause an alteration in their bandgap, which makes them potential materials for numerous applications. Perovskite microrods (MRs), nanorods (NRs), or nanowires (NWs) can provide better performances in different OE applications because of their unique crystal structure and tunable bandgap. One-dimensional (1D) OMPs have become quite popular due to better photovoltaic performance and other OE applications [4].

Im et al. have first synthesized the CH₃NH₃PbI₃ (MAPI) NWs in 2015 via a two-step spin-coating technique with a variation of DMF content [5]. They successfully demonstrated that the formation of MAPI NWs is more probable with a higher amount of DMF. The prepared NWs showed a fine absorption of visible wavelength, but the absorbance was slightly lower in comparison with bulk MAPI. In 2016, Spina

et al. also synthesized NWs of MAPI via slip-coating method for photodetection application [6]. This was a unique and one of the easiest methods for MAPI crystal growth. The process can avoid random nucleation, hence, control the crystal growth. They have not demonstrated the visible light absorption properties of this 1D MAPI. Wu et al. in 2018 have also studied the effect of DMF amount present in MAPI on the formation of 1D MAPI [7]. They successfully showed that at 1D, MAPI could be obtained via increasing the DMF contents. They also demonstrated the higher absorption properties of OMP NWs than 3D MAPI. This study disproves the low absorption of 1D MAPI as reported by Im et al. [5]. In 2019, Mishra et al. synthesized MAPI MRs by cooling down MAPI precursor solution to room temperature [8]. They reported that MAPI MRs could parallelly join, forming a long wire. But the MR growth process is rather slow, and no optical properties of the MRs had been observed for OE applications. Zhang et al. reported $CH_3NH_3PbBr_3$ MR synthesis in 2019 through the dip-coating technique for dynamically switchable microlaser [9]. However, fine absorption was obtained only in the wavelength below 550 nm.

Research on composite perovskites also got the attention of scientists. Various materials such as composites have been added with pure perovskite structure to get better performance and stability. Among them, perovskite composite with metal sulfide is a new direction of research to enhance optical performance, which was started in 2017. Chen et al. reported a MAPI : CdS film for SCs prepared via precursor blending method, which showed a better photovoltaic performance [10]. The absorbance was slightly increased between 500 nm and 750 nm in presence of CdS suggesting an increase in absorption coefficient. However, Cd is a highly toxic material and should be avoided. In 2019, Wang et al. synthesized PbS quantum dots embedded in MAPI NWs for photodetection application [11]. The composite nanorods showed better absorbance in a wide range of the visible spectrum than pure MAPI rods. These achievements uncovered that incorporating metal sulfide in OMPs can offer more enhanced optical performance, opening an alternative route in perovskite research and motivating us to conduct our research.

For deposition of thin film, numerous methods have been established, e.g., sol-gel spin coating, chemical vapor deposition (CVD), chemical bath, spray pyrolysis, and so on [12]. The sol-gel method can provide better crystallization with enhanced homogeneity at a relatively low temperature [13]. Though thermal evaporation, sputtering, CVD can provide better uniformity of the thin film, these methods are costly compared to spray pyrolysis, chemical bath, spin-coating, or doctor-blade methods. Among these economical methods, spin coating can provide better homogeneity for a small area of fabrication of thin film with minimal thickness [14]. Due to the simplicity and cost-effectivity, the spin coating is a favorable deposition method of perovskites.

Here, we report the synthesis of MAPI : ZnS MRs via a one-step spin-coating method. ZnS is also a potential material for OE applications with a high absorption coefficient [15], which has been used as ETL in PSCs, showing better

photovoltaic performance with a PCE of 17.4% [16]. To our best knowledge, various OE properties of MAPI : ZnS material have never been studied before. Here, we demonstrated the growth of MAPI : ZnS MRs in thin films and reported various structural, morphological, and optical alterations due to the variation in ZnS stoichiometry.

2. Experimental Details

2.1. Materials. Methylamine (MA) solution 33wt% (Sigma-Aldrich), hydroiodic acid (HI) 57% (Sigma-Aldrich), PbI_2 99% (Sigma-Aldrich), diethyl ether, N, N-dimethylformamide (DMF), zinc chloride (Merck), and thiourea (Merck) were used in this research process.

2.2. Preparation of MAPI and MAPI : ZnS Crystals. The synthesis process of CH_3NH_3I (MAI) was followed by previous research [17]. MA and HI solution of (1 : 1) molar ratio was mixed and stirred in an ice bath for 1 hour and further kept in the bath for 2 h. The solution was dried in an oven at 60°C, and the MAI crystal was formed, which was washed several times with diethyl ether to remove impurities. PbI_2 and MAI were completely dissolved in DMF at an equimolar ratio and dried at 60°C to obtain MAPI crystals. Figure 1 shows the prepared MAPI crystals. The precursor blending solution method was used to prepare MAPI : ZnS crystals [10]. $ZnCl_2$ and thiourea were dissolved by a 1 : 1 molar ratio in the MAPI-DMF solution and stirred for 30 minutes and evaporated in the oven at 60°C. MAPI : ZnS with three different molar ratios (e.g., 1 : 0.025, 1 : 0.05, and 1 : 0.1) were prepared. The pH of the MAPI, MAPI : ZnS (1 : 0.025), MAPI : ZnS (1 : 0.025), and MAPI : ZnS (1 : 0.025) solutions are, respectively, 6.11, 6.11, 6.12, and 6.13.

2.3. Thin-Film Preparation. MAPI and MAPI : ZnS precursor solutions of 0.5 gm/ml were prepared with DMF solvent. The viscosities of the MAPI, MAPI : ZnS (1 : 0.025), MAPI : ZnS (1 : 0.025), and MAPI : ZnS (1 : 0.025) solutions are measured to be 6.2822 mPa-s, 6.2782 mPa-s, 6.2731 mPa-s, and 6.2694 mPa-s, respectively. The glass substrates were cleaned with deionized water, ethanol, and acetone via ultrasonic cleaner. Preheated substrates were spin coated with a few drops of prepared solution at 1,500 rpm for 30 sec and then annealed at 80°C for 30 minutes. Figure 2 shows the prepared MAPI and MAPI : ZnS thin films.

2.4. Characterization. The X-ray diffraction (XRD) and Fourier transform infrared (FTIR) spectroscopy analyses were performed for all the prepared samples via Explorer diffractometer and IRPrestige-21, respectively, at Wazed Miah Science Research Centre (WMSRC), Jahangirnagar University (JU), Savar, Dhaka 1342, Bangladesh. The thin-film thickness was measured by the DektaXT-A surface profilometer at the Bangladesh Council of Scientific and Industrial Research (BCSIR), Dhanmondi, Dhaka 1205, Bangladesh. UV-Vis spectroscopy and SEM were also performed at BCSIR via UH4150 spectrophotometer and ZEISS
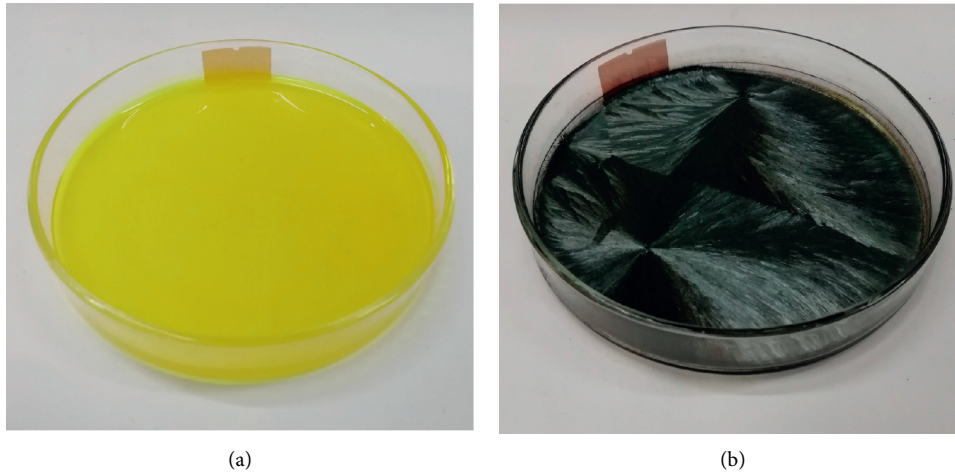
(a) (b)

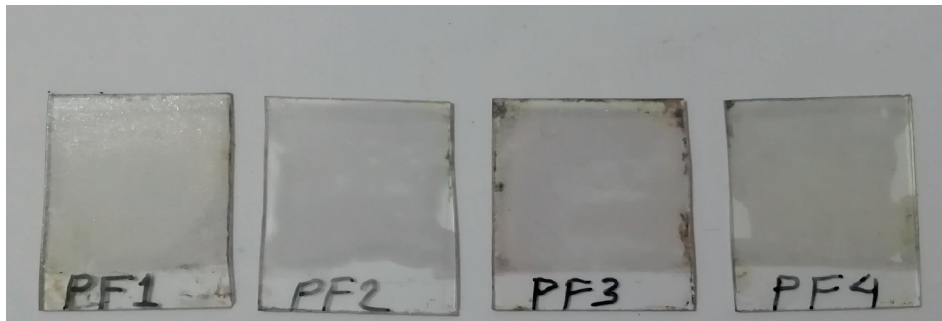Figure 1: (a) MAPI solution in DMF and (b) MAPI dried crystals.

Figure 2: Thin films of (a) MAPI, (b) MAPI : ZnS (1 : 0.025), (c) MAPI : ZnS (1 : 0.05), and (d) MAPI : ZnS (1 : 0.1) prepared by one-step spin-coating method.

EVO 18 SEM, respectively. Wayne Kerr 6500B Impedance Analyzer was used to measure the electrical resistance.

3. Result and Discussion

3.1. XRD Analysis. Figure 3 shows the XRD patterns for the samples MAPI and ZnS-doped MAPI. The diffraction peaks for MAPI were observed at 2θ values of 14.09°, 19.88°, 24.46°, 28.32°, 31.8°, 34.9°, 40.50°, and 43.07° and correspond to (100), (110), (111), (200), (102), (112), (202), and (212) planes, respectively, which satisfy previous report [18]. The addition of ZnS causes a structural deformation in the MAPI crystals, which is observed from the spectra exhibiting a slight shifting of the diffraction peaks toward higher 2θ values and from the lattice parameters, as shown in Table 1. The slight shifting toward higher 2θ indicates the increase in structural stress and decrease in interplanar spacing, which can cause the shrinkage of lattice [19]. No clear peaks of ZnS have been observed in the XRD spectra. However, an overlapped peak with the perovskite peak at 28.15° and a new peak at 32.68° in Figure 3 are analogous with ZnS's

corresponding peaks according to the Crystallography Open Database (COD ID - 1539414).

The absence of $ZnCl_2$ peaks can verify the formation of ZnS in the perovskite sample since ZnS was formed through the chemical reaction of $ZnCl_2$ and thiourea ($ZnCl_2 + CH_4N_2S = ZnS + CH_4N_2 + Cl_2$). The variation of ZnS concentration in the sample causes deformation in the perovskite's unit cell structure, as shown in Table 1. The overall cell volume of MAPI decreases with increasing ZnS concentration. The XRD peaks slightly broadened after ZnS incorporation, which represents a reduction in crystallite size and an increase in lattice defects [19].

3.1.1. Crystallite Size and Lattice Strain. A crystallite is a small region in a material made up of a single crystal, i.e., atomic regularity is exactly maintained in the region. On the other hand, lattice strain measures the distribution of lattice parameters resulting from imperfections and lattice dislocation in a crystal. Both crystallite size and lattice strain affect the Bragg peaks through broadening and shifting. The
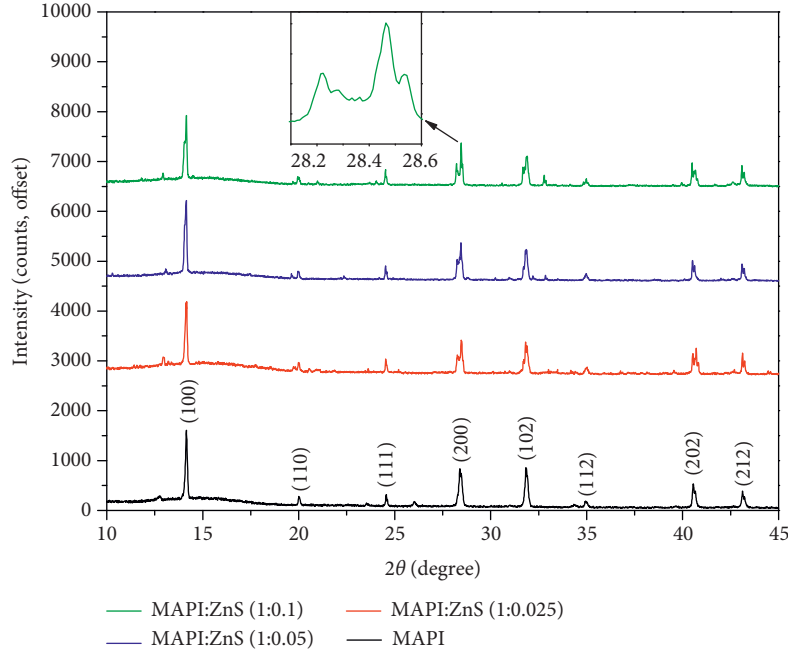
Figure 3: XRD spectra of MAPI and MAPI : ZnS thin films.

Table 1: Lattice parameters of MAPI and MAPI : ZnS crystals.

Material	Lattice parameters (Å)			Phase ($\alpha = \beta = \gamma = 90°$)	Cell volume (Å^3)
	a	b	C		
MAPI	6.3095	6.3095	6.280	Tetragonal	250.01
MAPI: ZnS (1 : 0.025)	6.300	6.300	6.2590	Tetragonal	248.42
MAPI: ZnS (1 : 0.05)	6.2941	6.2941	4.4720	Tetragonal	177.16
MAPI: ZnS (1 : 0.1)	4.4568	4.4568	6.2811	Tetragonal	124.76

crystallite sizes and lattice strains are calculated from equations (1) and (2) [20–22] and are listed in Table 2.

$$D = \frac{\kappa \lambda}{\Gamma \cos \theta}, \tag{1}$$

$$\xi = \frac{\Gamma}{4 \tan \theta}. \tag{2}$$

Here, D, ξ, Γ, κ, and λ are crystallite size, lattice strain, full-width half maxima, Scherrer constant (=0.9), and X-ray wavelength [20–22]. From the calculations, it was observed that the average crystallite size decreased with the increase in ZnS concentration (Figure 4). The presence of Zn or S atoms in the perovskites can cause irregularities and defects during the MAPI crystal growth. This can cause a reduction in average crystallite size. The lattice strain increases with increasing ZnS concentration. The increased strain represents higher stress due to the incorporation of foreign atoms. These stress and strain can also rise due to lattice mismatch, i.e., dissimilarity in the lattice structure of MAPI and the substrate and due to the difference in thermal expansion coefficients (α_L) between the film and substrate (α_L for MAPI is 43.3–33.3×10^{-6} K^{-1} and for the soda-lime substrate is 9×10^{-6} K^{-1}) [23, 24].

3.1.2. Dislocation Density and Stacking Fault. The dislocation density (ρ_d) represents the total dislocation length per unit volume in a crystalline material, which denotes irregularities and material strength. Generally, a material with a higher dislocation density offers increased strength [25]. On the other hand, stacking faults (S_F) are abnormalities in the crystal plane stacking sequence that violate the ideal lattice's regularity [26]. The dislocation density and stacking fault were calculated from equations (3) and (4) [27, 28].

$$\rho_d = \frac{1}{D^2}, \tag{3}$$

$$S_F = \frac{2\pi^2 \Gamma}{45 \, (3 \tan \theta)^{1/2}}, \tag{4}$$

where D and Γ are the crystallite size and full-width half maxima, respectively. Both ρ_d and S_F increase with ZnS concentration, which signifies that the presence of ZnS increases defects in the MAPI crystal growth. These increased defects can be identified as the cause of the reduction in average crystallite size. The increased value of ρ_d represents lower crystallinity of the material, i.e., the overall crystallinity decreased after ZnS addition. This also signifies that MAPI : ZnS (1 : 0.1) possesses higher strength compared to pure MAPI.

TABLE 2: Average crystallite size, lattice strain, dislocation density, and stacking fault of MAPI and MAPI : ZnS.

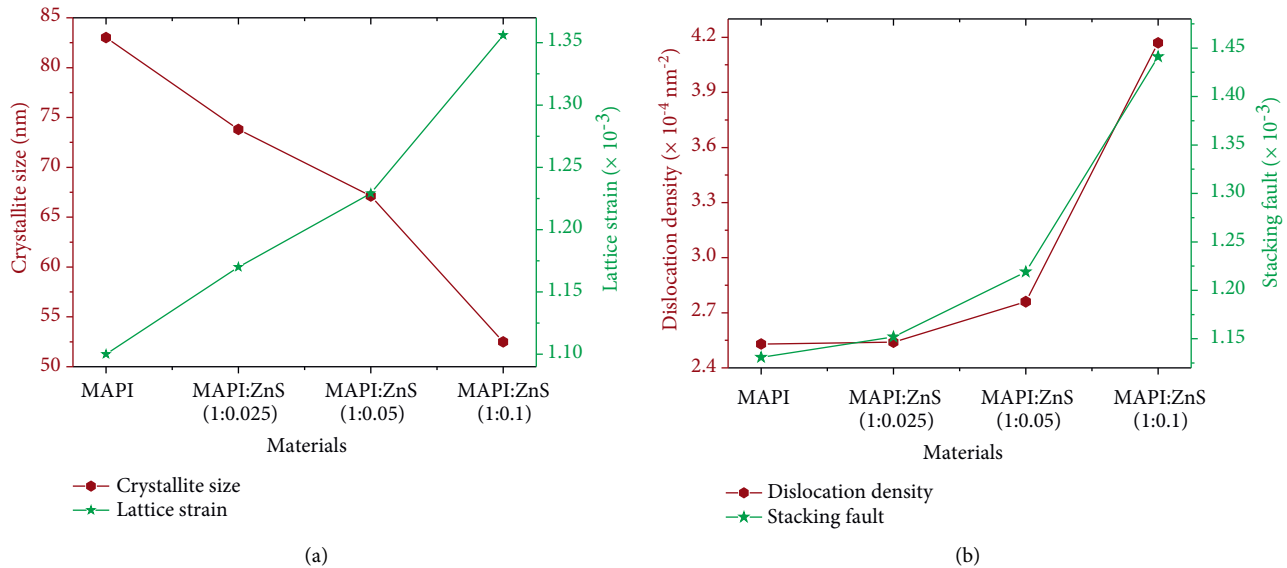| Material	Average crystallite size (nm)	Average lattice strain ($\times 10^{-3}$)	Dislocation density ($\times 10^{-4}$ nm^{-2})	Stacking fault ($\times 10^{-3}$)
MAPI	83.02	1.10	2.50	1.13
MAPI: ZnS (1 : 0.025)	73.80	1.18	2.54	1.15
MAPI: ZnS (1 : 0.05)	37.13	1.23	2.76	1.22
MAPI: ZnS (1 : 0.1)	52.50	1.36	4.17	1.44

(a)

(b)

FIGURE 4: (a) Average crystallite size and lattice strain, and (b) dislocation density, stacking fault of MAPI, and MAPI : ZnS.

3.2. FTIR Analysis.

FTIR spectra were observed in the wavenumber range 750 cm^{-1}–4,000 cm^{-1} (Figure 5) for pure perovskite and perovskite:ZnS crystals. The broad peak between 3,455 cm^{-1} and 3687 cm^{-1} represents O-H stretching due to the presence of moisture in the samples. The peaks of very less intensity at 3,187 cm^{-1} are of NH$_3^+$ asymmetric stretching and at 3,130 cm^{-1} are of NH$_3^+$ symmetric stretching. CH$_3$ asymmetric stretching and symmetric stretching were observed at 2,958 cm^{-1} and 2,918 cm^{-1}, respectively [29]. The peaks at 1,585 cm^{-1}, 1,460 cm^{-1}, and 1,422 cm^{-1} are due to asymmetric NH$_3^+$ bending, symmetric NH$_3^+$ bending, and CH$_3$ bending, respectively [30]. The peak at 1,020 cm^{-1} represents C-N stretching [31]. The peaks at 1,255 cm^{-1} and 944 cm^{-1} represent CH$_3$-NH$_3^+$ rocking [32]. Due to the transparency of PbI$_2$ to infrared wavelength, no peak for Pb-I was observed in the spectrum [33].

For small stoichiometry of the ZnS mixture in the sample, very slight changes in the peak position were observed. But after reaching the molar ratio of MAPI and ZnS to 1 : 0.1, all the peak positions significantly change due to the structural deformation. NH$_3^+$ stretching peaks were observed at 3,193 cm^{-1} (asymmetric) and 3,139 cm^{-1} (symmetric). The peaks at 2,948 cm^{-1}, 1,467 cm^{-1}, and 1,010 cm^{-1} define CH$_3$ stretching, CH$_3$ bending, and C-N stretching. Both peaks of CH$_3$-NH$_3^+$ rocking shifted to 1,250 cm^{-1} and 954 cm^{-1}. A new peak at 1,099 cm^{-1} arises with ZnS increment, which can be identified as the characteristic peak of ZnS [34]. Again, a strong peak at 1,625 cm^{-1} was observed, previously characterized as the absorption of inorganic sulfide compounds [35].

3.3. Surface Morphology.

Figure 6 shows the SEM images of pure perovskite and perovskite: ZnS MRs in the thin films. MAPI crystals generally grow through a dendrite structure; this dendrite formation allows perovskite to uniformly extend in a particular direction, which finally takes the form of wires or rods [36]. MAPI MR formation is observed in the thin film with an average rod diameter of about 612 nm.

After the addition of ZnS, porosity was observed in the perovskite structures. The rod structure started to break down and transformed into the smaller irregular-sized grain with ZnS increment. Some of the ZnS may have formed in the path of MAPI crystal growth, which opposed the further crystal growth. Hence, the grain size decreased and porosity increased. In Figures 6(c)–6(d), the change in grain structure with the increments of ZnS constituent in the samples is clearly observed. The average diameter of the irregular grains, finally observed, is 508 nm.

3.4. Elemental Analysis.

Figure 7 shows the energy-dispersive X-ray (EDX) spectra of the prepared thin films. The EDX analysis reveals the presence of C, N, Pb, I, Zn, and S atoms in the samples. In the targeted area of MAPI and MAPI : ZnS thin films, the atomic ratios of Pb/I are
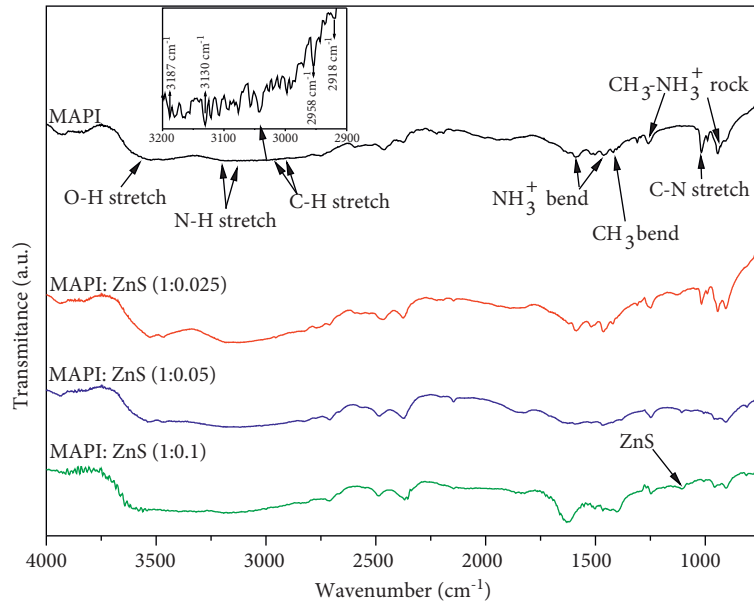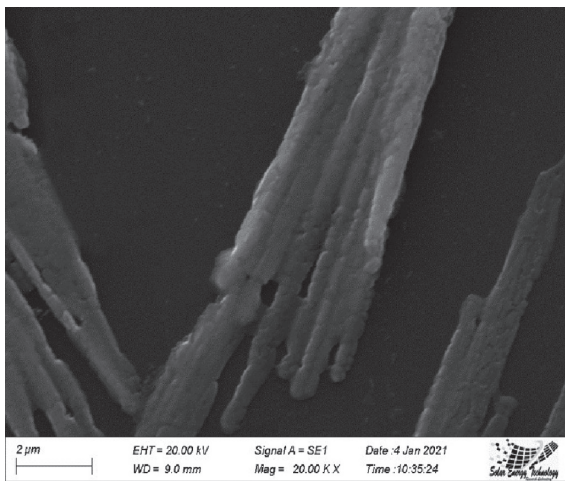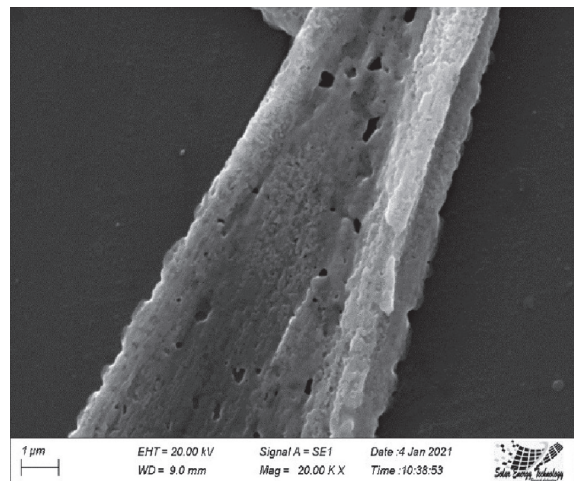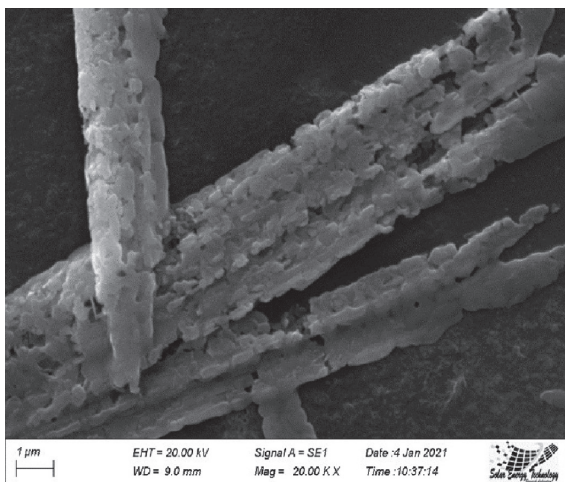
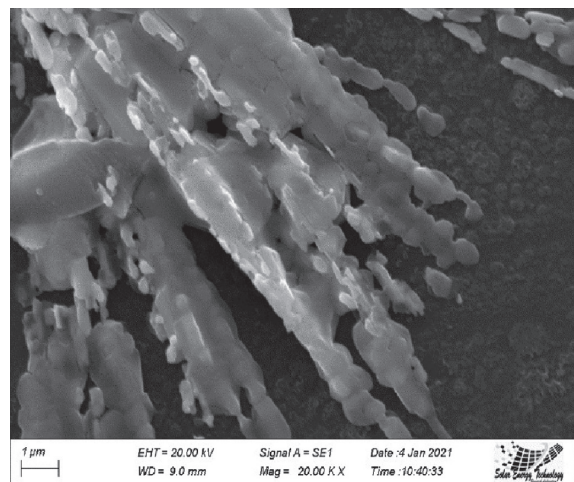Figure 5: FTIR spectra of MAPI and MAPI: ZnS MRs.

(a)

(b)

(c)

(d)

Figure 6: SEM images of (a) MAPI, (b) MAPI: ZnS (1 : 0.025), (c) MAPI: ZnS (1 : 0.05), and (d) MAPI: ZnS (1 : 0.1) thin films.
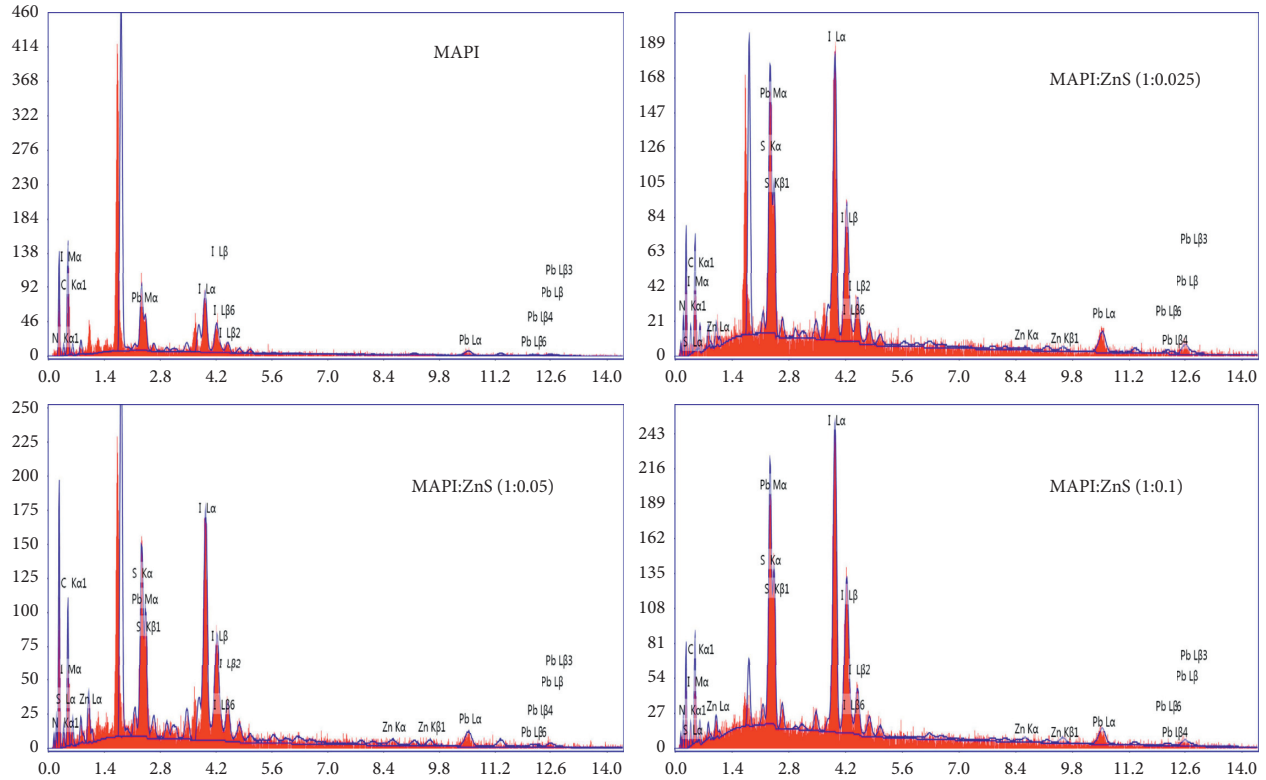
Figure 7: EDX spectra of the MAPI and MAPI : ZnS thin films.

0.42, 0.35, 0.32, and 0.30, which are close to previous reports [37, 38]. According to a previous report, MAPI is very sensitive toward high-energy electron beams and easily decomposes through the EDX analysis process, which causes variations in the Pb/I ratio [39].

The increment of Zn and S atoms in the films is observed with the sequential order maintaining the atomic ratio of Zn/S between 0.83 and 0.97. The atomic % and weight % of the different elements observed in the EDX spectra are listed in Table 3.

3.5. Optical Characteristics. The UV-visible absorption was analyzed in the wavelength range of 400 nm–900 nm for each thin film. Figure 8 shows the absorption spectrum of the prepared thin films. As observed in earlier reports, the MAPI film showed a fine absorption in the visible and near-infrared wavelength range [40, 41]. The absorption onset for pure MAPI thin film is about 800 nm, consistent with the report of Tombe et al. [41]. The absorbance edge shifted to short-wavelength values as the ZnS concentration increased, suggesting that the bandgap energy of the produced perovskite thin films increased. The absorption spectrum follows blue shifting with further increasing ZnS concentration in the sample. The reason is that ZnS shows strong absorption in the short-wavelength region [42, 43].

The absorption coefficients (α) shown in Figure 9 of the thin films are calculated using the following equation [44]:

$$\alpha = \frac{2.303A}{t}, \tag{5}$$

where A is the absorbance and t is the film thickness measured by the surface profilometer. The MAPI film had an absorption coefficient above $10^4 \, \text{cm}^{-1}$, making it a potential candidate for numerous OE applications, especially for the SC absorber layer [45]. The absorption coefficient increased with the increase in ZnS concentration and reached up to the order of $10^5 \, \text{cm}^{-1}$. The absorption coefficient edge is blue shifted with the rise of ZnS concentration in MAPI thin film. This phenomenon occurred because ZnS has a high absorption coefficient in the low wavelength range [15, 46]. The values of α for pure MAPI at 400 nm and 750 nm are $7.7 \times 10^4 \, \text{cm}^{-1}$ and $6.9 \times 10^4 \, \text{cm}^{-1}$, respectively. The electromagnetic waves of 400 nm and 750 nm have a penetration depth (δ) of 0.13 μm and 0.14 μm, respectively, which means 37% of the incidents at 400 nm and 750 nm wavelengths are absorbed after traversing 0.13 μm and 0.14 μm thickness of the film, respectively. On the other hand, for MAPI : ZnS (1 : 0.1) thin film, α is $1.08 \times 10^5 \, \text{cm}^{-1}$ and $4.1 \times 10^4 \, \text{cm}^{-1}$ for 400 nm and 750 nm wavelengths, respectively. The corresponding penetration depths are 0.1 μm and 0.25 μm, i.e., only a few micron thick films are sufficient to absorb most of the visible spectrum.

The reflectance spectra of the thin films are shown in Figure 10. The reflectance is very low (<7.5%) for all the samples and slightly varies very in the visible wavelength range. This less reflectance corresponds to minor energy loss due to reflection. The overall reflectance of the thin films

TABLE 3: Elemental atomic % and weight % measure via EDX spectroscopy.

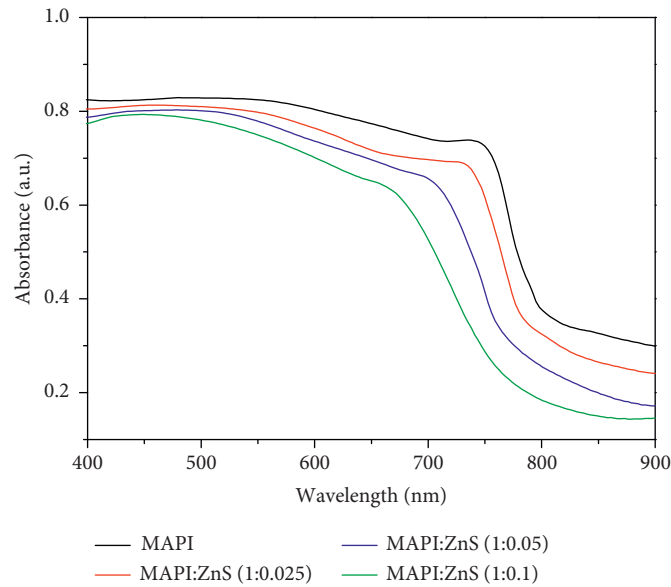| Elements		Materials			
		MAPI	MAPI : ZnS (1 : 0.025)	MAPI : ZnS (1 : 0.05)	MAPI : ZnS (1 : 0.1)
C	Weight %	23.56	9.18	7.38	19.02
	Atomic %	64.64	46.02	40.81	65.01
N	Weight %	8.74	4.08	3.51	4.05
	Atomic %	20.56	17.53	16.64	11.87
Pb	Weight %	27.55	31.21	28.53	25.64
	Atomic %	4.38	9.07	9.15	5.08
I	Weight %	40.15	54.24	58.58	48.5
	Atomic %	10.43	25.73	30.66	15.69
Zn	Weight %	—	0.81	1.33	1.87
	Atomic %	—	0.75	1.35	1.17
S	Weight %	—	0.48	0.67	0.92
	Atomic %	—	0.9	1.39	1.18

FIGURE 8: Absorbance spectra of the prepared thin films.

increased with increasing ZnS concentration. This observation represents the reduction in crystallite size and the increase in imperfection since crystal imperfection can increase the scattering of photons [47]. Overall low reflectance indicates that the loss of incident energy due to reflection is very less, which is preferable to OE applications. These materials with low reflectivity are suitable for various antireflection coating in optical devices.

The refractive index (η) is an essential optical property for the solar cell absorber layer. A higher refractive index corresponds to higher reflectivity and lesser PCE for solar cells. Materials with a low value of η are very suitable for SC absorber material and an antireflection layer. The refractive index of the thin films was calculated from the following equation [48],

$$\eta = \frac{1 + R}{1 - R} + \sqrt{\frac{4R}{(1 - R)^2} - \left(\frac{\alpha\lambda}{4\pi}\right)^2}, \tag{6}$$

where R, λ, and α are the reflectance, incident wavelength, and absorption coefficient, respectively. Figure 11 shows the variation of η with increasing wavelength. The value of η is very low (1.48–1.67) for all the thin films. The refractive index of MAPI is comparatively low in the visible region and decreased after ZnS incorporation, reducing the energy loss due to reflection and improving the optical performance. For each thin film, the refractive index decreases with increasing wavelength in the visible region and then increases with increasing wavelength in the longer wavelength region. This suggests that longer wavelengths are reflected more from the materials in comparison to the visible wavelength. At higher wavelengths, η slightly increases with the increase in ZnS stoichiometry.

The bandgap of the films was calculated via Tauc relation [49] involving absorption coefficient (α) and photon energy given by the following equation:

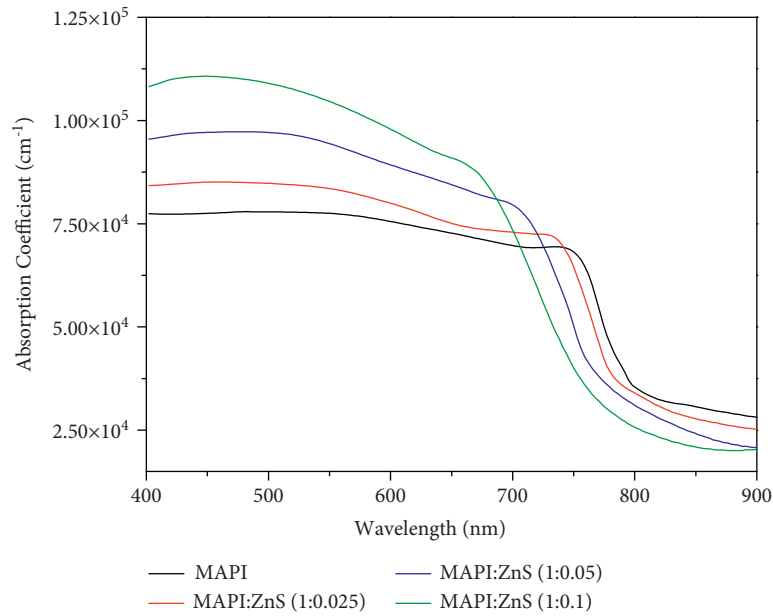$$\alpha h\nu = A\left(h\nu - E_g\right)^n, \tag{7}$$

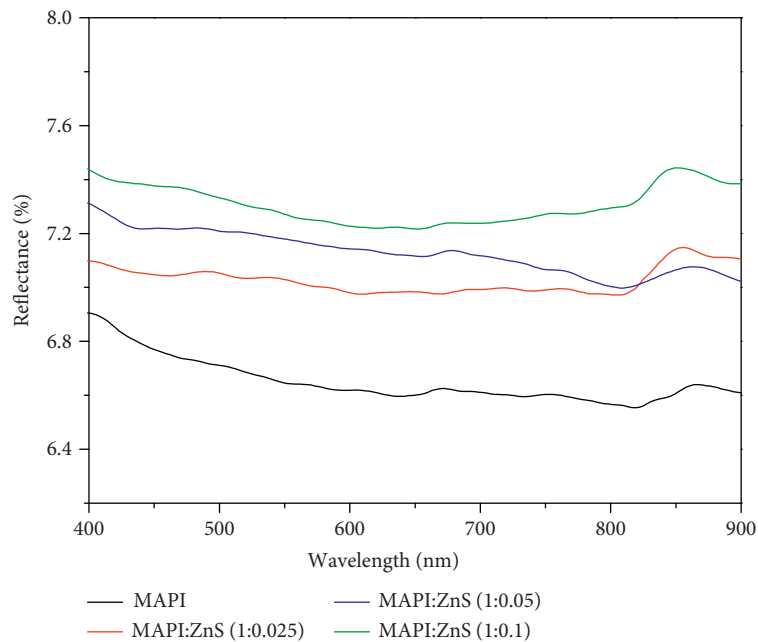FIGURE 9: Absorption coefficients of the prepared thin films.

FIGURE 10: Reflectance spectra of the prepared thin films.

where A, h, ν, and E_g are constant called band-tail parameter, Planck's constant, frequency of the photon, and bandgap, respectively. Tauc plot is plotted in Figure 12, which revealed the bandgap MAPI thin film about 1.55 eV, satisfying the previous report [41]. The incorporation of ZnS caused to increase in the bandgap energy from 1.55 eV to 1.64 eV with increasing ZnS concentration. Obtained optical bandgaps are shown in Table 4.

The XRD result shows that the lattice parameters and unit cell volume decreased with the increasing ZnS ratio in the MAPI samples. Due to the decrease in lattice parameters,

molecules become more closely packed in the presence of ZnS; hence, the electrons are more strongly bound in the lattice. Consequently, more energy will be required to free the electrons from the valance band (VB) due to the increase in the electron's binding energy with parent atoms, meaning the bandgap increases. The decrease in lattice parameter also represents the decrease in bond length. As a result, the energy gap between bonding orbital and antibonding orbital increases, which also indicates the increase in the bandgap. It is also observed that the average crystallite size decreased from 83.02 nm to 53.5 nm, which can also be a reason for
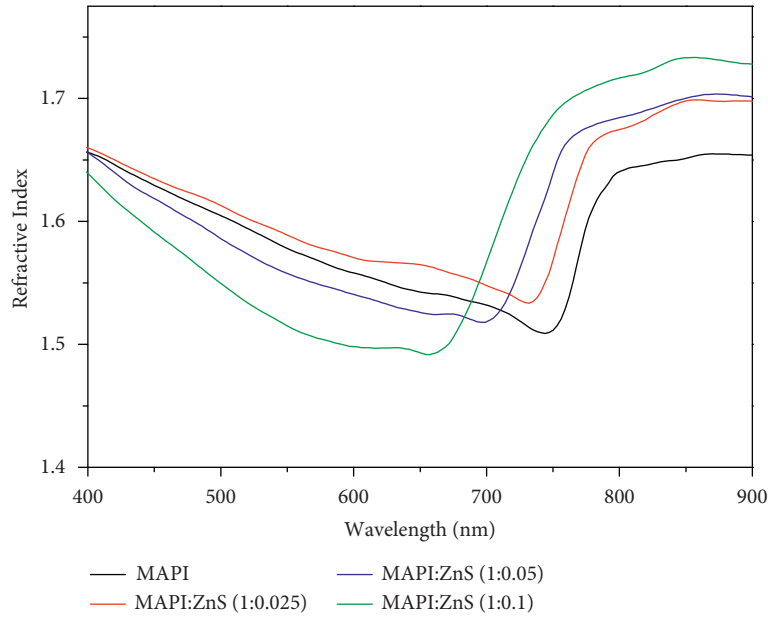
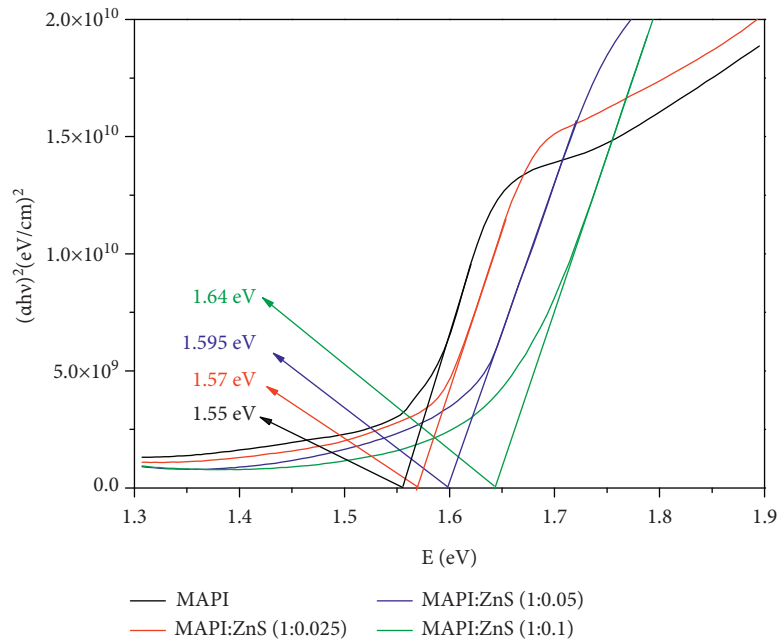FIGURE 11: Refractive index of the thin films.

FIGURE 12: Tauc plot for MAPI and MAPI: ZnS thin films.

bandgap increment due to quantum confinement [50]. The obtained bandgaps are highly preferable for absorbing the visible light spectrum.

Figure 13 shows the optical conductivity (OC) variation with respect to incident photon energies for all prepared samples. The OC was calculated using the following equation [44]:

$$\sigma = \frac{\alpha \eta c}{4\pi}, \tag{8}$$

where σ, η, c, and α are optical conductivity, refractive index, speed of light, and thin-film absorption coefficient,

respectively. Optical conductivity represents the rise of conductive property in the presence of light. Electron-hole pairs can be generated through the absorption of photon energy, which increases the electrons in CB and holes in VB. Hence, the conductivity increases. In MAPI thin film, OC increased with the incident photon energy.

The incorporation of ZnS increased the absorption coefficient resulting in a boost of free carriers. The increase in free carriers can lead to the increase in OC of the thin films [51]. The variation of σ with photon energy showed an almost similar nature with a blue shifting of spectrum edge

TABLE 4: Bandgap variation in the optical and electrical methods.

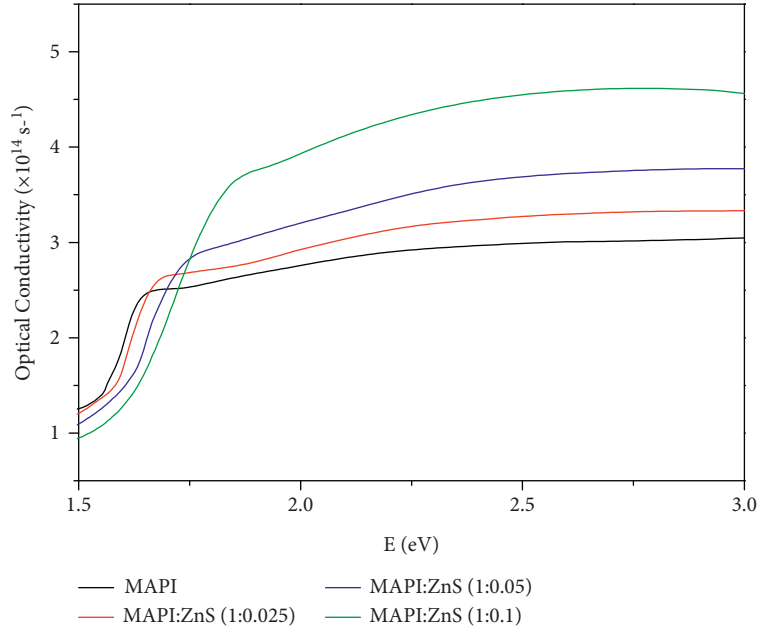| Materials	Slope (β)	ε_g (eV)	E_g (eV)
MAPI	8757.99	1.511	1.55
MAPI : ZnS (1 : 0.025)	8959.49	1.546	1.57
MAPI : ZnS (1 : 0.05)	9091.51	1.569	1.595
MAPI : ZnS (1 : 0.1)	9380.72	1.619	1.64

FIGURE 13: Optical conductivity of the thin films.

with the increase in ZnS stoichiometry. The OC blue shifted due to the decrease in cell volume and crystallite size, which increase the bandgap. As a result, more photon energy is required for electron transition from VB to CB. All the films showed higher OC of the order of $10^{14}\,\mathrm{s}^{-1}$. The increased σ suggests that the material MAPI : ZnS is much potential material for various OE (e.g., SCs and photodetector) applications.

3.6. Temperature Variation of Resistance.

Figure 14 shows the variation of the film's electrical resistance (R) with respect to operating temperatures (T). Due to the negative temperature coefficient of resistivity (TCR), the resistance of the thin films decreased with increasing temperature, that is, with increasing temperature, more valance electrons gain energies to overcome the bandgap and become conduction electrons. This means that with the increase in temperature, the carrier concentration also increases; hence, the resistance decreases. The resistance increased with the ZnS molar concentration since the grain boundary resistance (R_{gb}) per unit length increased, reducing the cross transport of carriers [52].

The bandgap of a semiconductor can be measured from the temperature dependence of resistance. According to the band theory of solids, the relation between resistance and temperature is given by

$$R_T = R_p e^{\varepsilon_g/2kT}, \tag{9}$$

where ε_g, k, T, and R_T represent the energy gap between the top of VB and the bottom of CB, Boltzmann constant, Kelvin temperature, and electric resistance at temperature T. R_p is a temperature-independent resistance (constant). The above equation can be modified as follows:

$$\varepsilon_g = 2k \frac{\Delta \ln(R)}{\Delta T^{-1}} . \tag{10}$$

From the graph of ln(R) vs. T^{-1} as shown in Figure 14, the slope was determined, and finally, from equation (10), the bandgaps are calculated and listed in Table 4. It can be observed that the calculated values of bandgaps via electrical means are quite analogous with the ones obtained by Tauc relation containing slight deviations. In both cases, the bandgap energies increased via ZnS incorporation.
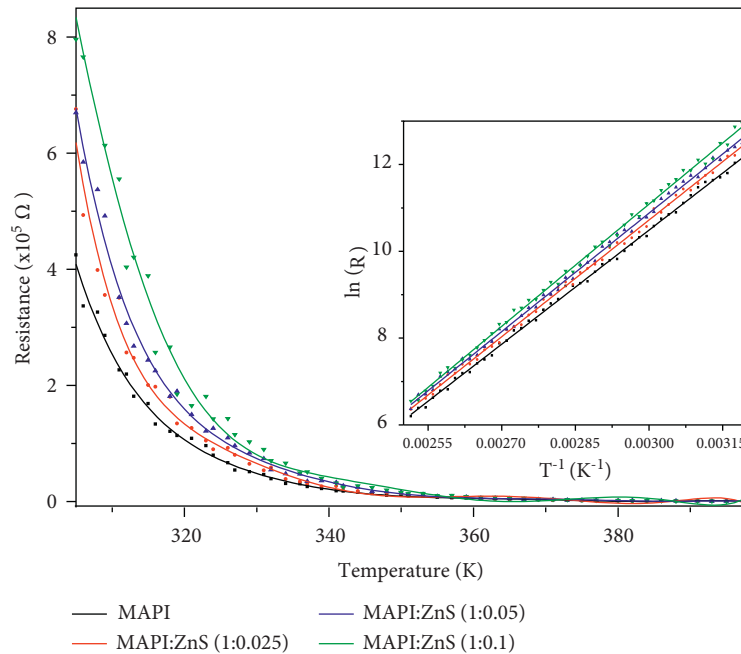
FIGURE 14: Temperature variation of resistance of the prepared MAPI films.

4. Conclusions

This study has demonstrated the successful synthesis of MAPI and MAPI : ZnS MRs with different molar ratios via the spin-coating method. Variation of ZnS molar ratio caused changes in morphological and optical properties of MAPI. The XRD and FTIR graphs show fine crystallinity and appropriate molecular vibrations present in the prepared samples. High absorption in the visible wavelength region with a tunable bandgap between 1.55 eV and 1.64 eV through varying ZnS stoichiometry in the MAPI was perceived. The bandgaps were obtained via the Tauc method and an electrical method, which showed similar results. This tunability of the bandgap can improve performance in various applications like solar cells, laser, and LEDs. All the observed properties, including very low reflectance between 1.48 and 1.64 and high absorption coefficient over 10^4 cm^{-1} in the visible and near-visible wavelength range proving that MAPI : ZnS MRs are potential candidates for different opto-electronics applications.

Data Availability

The data used to support the findings of this study have not been made available because they are still being used in ongoing research.

Conflicts of Interest

The authors declare that there is no conflict of interest regarding the publication of this article.

Acknowledgments

Supplementary Materials

Graphical abstract of the research article. s. (*Supplementary Materials*)

References

[1] J. Chen, S. Zhou, S. Jin, H. Li, and T. Zhai, "Crystal organometal halide perovskites with promising optoelectronic applications," *Journal of Materials Chemistry C*, vol. 4, pp. 11–27, 2016.

[2] D. Zhou, T. Zhou, Y. Tian, X. Zhu, and Y. Tu, "Perovskite-based solar cells: materials, methods, and future perspectives," *Journal of Nanomaterials*, vol. 2018, 2018.

[3] S. Chen, X. Zhang, J. Zhao et al., "Atomic scale insights into structure instability and decomposition pathway of methylammonium lead iodide perovskite," *Nature Communications*, vol. 91, no. 9, pp. 1–8, 2018.

[4] C. Zhang, D. Bin Kuang, and W. Q. Wu, "A Review of Diverse Halide Perovskite Morphologies for Efficient Optoelectronic Applications," *Small Methods*, vol. 4, pp. 1–30, 2020.

[5] J.-H. Im, J. Luo, M. Franckevičius et al., "Nanowire perovskite solar cell," *Nano Letters*, vol. 15, no. 3, pp. 2120–2126, 2015.

[6] M. Spina, E. Bonvin, A. Sienkiewicz, B. Náfrádi, L. Forró, and E. Horváth, "Controlled growth of CH3NH3PbI3 nanowires in arrays of open nanofluidic channels," *Scientific Reports*, vol. 6, no. 1, Article ID 19834, 2016.

[7] D. Wu, H. Zhou, Z. Song, R. Liu, and H. Wang, "The effect of N,N-dimethylformamide on MAPbI3 nanowires for

application in flexible photodetectors," *Journal of Materials Chemistry C*, vol. 6, no. 32, pp. 8628–8637, 2018.

[8] A. Mishra, Z. Ahmad, F. Touati, R. A. Shakoor, and M. K. Nazeeruddin, "One-dimensional facile growth of MAPbI3 perovskite micro-rods," *RSC Advances*, vol. 9, no. 20, Article ID 11589, 2019.

[9] N. Zhang, Y. Fan, K. Wang et al., "All-optical control of lead halide perovskite microlasers," *Nature Communications*, vol. 10, no. 1, p. 1770, 2019.

[10] C. Chen, Y. Zhai, F. Li et al., "High efficiency CH3NH3PbI3: CdS perovskite solar cells with CuInS2 as the hole transporting layer," *Journal of Power Sources*, vol. 341, pp. 396–403, 2017.

[11] R. Wang, F. Wang, W. Zhou et al., "Colloidal-quantum-dot-in-perovskite nanowires," *Infrared Physics & Technology*, vol. 98, pp. 16–22, 2019.

[12] M. B. Zaman, T. Chandel, and K. Dehury, "Synthesis and characterization of spin-coated ZnSThin films," *AIP Conference Proceedings*, vol. 1953, p. 100066, 2018.

[13] D. Navas, S. Fuentes, A. Castro-Alvarez, and E. Chavez-Angel, "Review on sol-gel synthesis of perovskite and oxide nanomaterials," *Gels*, vol. 7, no. 4, p. 275, 2021.

[14] A. Boudrioua, M. Chakaroun, and A. Fischer, "Organic light-emitting diodes," in *Organic Lasers*, pp. 49–93, Elsevier, Chennai, Tamil Nadu, 2017.

[15] A. H. O. Al-Khayatt and M. D. Jaafer, "Characteristics of Nanocrystalline ZnS thin films grown on glass with different Zn ion concentrations by CBD technique," *IOSR Journal of Applied Physics*, vol. 6, no. 1, pp. 27–35, 2014.

[16] C. C. Tseng, G. Wu, L. B. Chang et al., "Effects of Annealing on Characteristics of Cu2ZnSnSe4/CH3NH3PbI3/ZnS/IZO Nanostructures for Enhanced Photovoltaic Solar Cells," *Nanomaterials*, vol. 10, pp. 1–16, 2020.

[17] A. Kojima, K. Teshima, Y. Shirai, and T. Miyasaka, "Organometal halide perovskites as visible-light sensitizers for photovoltaic cells," *Journal of the American Chemical Society*, vol. 131, pp. 6050-6051, 2009.

[18] D. Ju, T. Zhao, D. Yangyang et al., "Gas induced conversion of hybrid perovskite single crystal to single crystal for great enhancement of their photoelectric properties," *Journal of Materials Chemistry*, vol. 5, no. 41, Article ID 21919, 2017.

[19] H. Benamra, H. Saidi, A. Attaf, M. S. Aida, A. Derbali, and N. Attaf, "Physical properties of Al-doped ZnS thin films prepared by ultrasonic spray technique," *Surfaces and Interfaces*, vol. 21, Article ID 100645, 2020.

[20] A. Göktaş, A. Tumbul, and F. Aslan, "Grain size-induced structural, magnetic and magnetoresistance properties of Nd0.67Ca0.33MnO3 nanocrystalline thin films," *Journal of Sol-Gel Science and Technology*, vol. 78, pp. 262–269, 2016.

[21] G. Balakrishnan, V. Sinha, Y. P. Peethala et al., "Structural and optical properties of ZnO thin film prepared by sol-gel spin coating," *Materials Science-Poland*, vol. 38, no. 1, pp. 17–22, 2020.

[22] M. M. El-Desoky, G. A. El-Barbary, D. E. El Refaey, and F. El-Tantawy, "Optical constants and dispersion parameters of La-doped ZnS nanocrystalline films prepared by sol-gel technique," *Optik*, vol. 168, pp. 764–777, 2018.

[23] S. Logunov, S. Marjanovic, and J. Balakrishnan, "Laser assisted frit sealing for high thermal expansion glasses," *Journal of Laser Micro/Nanoengineering*, vol. 7, no. 3, pp. 326–333, 2012.

[24] Y. Rakita, S. R. Cohen, N. K. Kedem, G. Hodes, and D. Cahen, "Mechanical properties of APbX3 (A = Cs or CH3NH3; X= I or Br) perovskite single crystals," *MRS Communications*, vol. 5, no. 4, pp. 623–629, 2015.

[25] A. Muiruri, M. Maringa, and W. du Preez, "Evaluation of Dislocation Densities in Various Microstructures of Additively Manufactured Ti6Al4V (Eli) by the Method of X-ray Diffraction," *Materials*, vol. 13, pp. 1–23, 2020.

[26] S. Sturm and B. Jančar, "Microstructure characterization of advanced ceramics," in *Advanced Ceramics for Dentistry*, pp. 151–172, Elsevier Inc, Amsterdam, Netherlands, 2014.

[27] M. Arslan, A. Habib, M. Zakria, A. Mehmood, and G. Husnain, "Elemental, structural and optical properties of nanocrystalline Zn 1−x Cu x Se films deposited by close spaced sublimation technique," *Journal of Science: Advanced Materials and Devices*, vol. 2, no. 1, pp. 79–85, 2017.

[28] A. Goktas, A. Tumbul, Z. Aba, A. Kilic, and F. Aslan, "Enhancing crystalline/optical quality, and photoluminescence properties of the Na and Sn substituted ZnS thin films for optoelectronic and solar cell applications; a comparative study," *Optical Materials*, vol. 107, Article ID 110073, 2020.

[29] T. Glaser, C. Müller, M. Sendner et al., "Infrared spectroscopic study of vibrational modes in methylammonium lead halide perovskites," *The Journal of Physical Chemistry Letters*, vol. 6, no. 15, pp. 2913–2918, 2015.

[30] J. Idígoras, A. Todinova, J. R. Sánchez-Valencia, A. Barranco, and J. A. Anta, "The interaction between hybrid organic-inorganic halide perovskite and selective contacts in perovskite solar cells: an infrared spectroscopy study," *Physical Chemistry Chemical Physics*, vol. 18, no. 19, pp. 13583–13590, 2016.

[31] A. B. D. Nandiyanto, R. Oktiani, and R. Ragadhita, "How to read and interpret FTIR spectroscope of organic material," *Indonesian Journal of Science and Technology*, vol. 4, no. 1, pp. 97–118, 2019.

[32] G. Abdelmageed, L. Jewell, K. Hellier et al., "Mechanisms for light induced degradation in MAPbI3 perovskite thin films and solar cells," *Applied Physics Letters*, vol. 109, no. 23, Article ID 233905, 2016.

[33] J. M. C. Da Silva Filho, V. A. Ermakov, and F. C. Marques, "Perovskite Thin Film Synthesised from Sputtered Lead Sulphide," *Scientific Reports*, vol. 8, pp. 1–8, 2018.

[34] M. Nikzad, M. R. Khanlary, and S. Rafiee, "Structural, optical and morphological properties of Cu-doped ZnS thin films synthesized by sol-gel method," *Applied Physics A*, vol. 125, no. 8, p. 507, 2019.

[35] P. V. Raleaooa, A. Roodt, G. G. Mhlongo, D. E. Motaung, R. E. Kroon, and O. M. Ntwaeaborwa, "Luminescent, magnetic and optical properties of ZnO-ZnS nanocomposites," *Physica B: Condensed Matter*, vol. 507, pp. 13–20, 2017.

[36] X.-D. Liu, Q. Wang, Z.-Q. Cheng, Y.-H. Qiu, L. Zhou, and Q.-Q. Wang, "Solution-phase growth of organolead halide perovskite nanowires and nanoplates assisted by long-chain alkylammonium and solvent polarity," *Materials Letters*, vol. 206, pp. 75–79, 2017.

[37] G. Liang, H. Lan, P. Fan et al., "Highly uniform large-area (100 cm2) perovskite CH3NH3PbI3 thin-films prepared by single-source thermal evaporation," *Coatings*, vol. 8, no. 8, p. 256, 2018.

[38] P. Fan, D. Gu, G.-x. Liang et al., "Growth of high quality CH3NH3PbI3 thin films prepared by modified dual-source vapor evaporation," *Journal of Materials Science: Materials in Electronics*, vol. 27, no. 3, pp. 2321–2327, 2016.

[39] S. Chen, X. Zhang, J. Zhao et al., *Nature Communications*, vol. 91, no. 9, pp. 1–8, 2018.

[40] J. Burschka, N. Pellet, S.-J. Moon et al., "Sequential deposition as a route to high-performance perovskite-sensitized solar cells," *Nature*, vol. 499, no. 7458, pp. 316–319, 2013.

[41] S. Tombe, G. Adam, H. Heilbrunner et al., "Optical and electronic properties of mixed halide (X = I, Cl, Br) methylammonium lead perovskite solar cells," *Journal of Materials Chemistry C*, vol. 5, no. 7, pp. 1714–1723, 2017.

[42] V. D. Mote, Y. Purushotham, and B. N. Dole, "Structural, morphological and optical properties of Mn doped ZnS nanocrystals," *Cerâmica*, vol. 59, no. 351, pp. 395–400, 2013.

[43] G. G. Ramteke, A. S. Lanje, D. M. Pimpalshende, fnm au, A. S. Lanje, and D. M. Pimpalshende, "Structural and optical performance of ZnS nanoparticles synthesized via chemical route," *International Journal of Scientific Research in Physics and Applied Sciences*, vol. 6, no. 3, pp. 69–74, 2018.

[44] A. Q. Abdullah, "Surface and volume energy loss, optical conductivity of rhodamine 6G dye (R6G)," *Chemistry and Materials Research*, vol. 3, p. 10, 2013.

[45] T. Unold and C. A. Kaufmann, *Chalcopyrite thin-film materials and solar cells*, Vol. vol. 1, Elsevier, , Chennai, Tamil Nadu, 2012.

[46] N.-A. Molland, Z. Ghadyani, E. A. Karhu et al., "Band-edge modification and mid-infrared absorption of co-deposited $Fe_xZn_{1-x}S$ thin films," *Optical Materials Express*, vol. 5, no. 7, p. 1613, 2015.

[47] P. Sivakumar, H. S. Akkera, T. Ranjeth Kumar Reddy, G. Srinivas Reddy, N. Kambhala, and N. Nanda Kumar Reddy, "Influence of Ga doping on structural, optical and electrical properties of transparent conducting SnO_2 thin films," *Optik*, vol. 226, Article ID 165859, 2021.

[48] Q. M. Al-Bataineh, A. A. Ahmad, A. M. Alsaad, and A. D. Telfah, "Optical characterizations of PMMA/metal oxide nanoparticles thin films: bandgap engineering using a novel derived model," *Heliyon*, vol. 7, no. 1, Article ID e05952, 2021.

[49] P. O. Offor, A. C. Nwanya, A. D. Omah et al., "Chemical spray pyrolysis deposition of zinc sulphide thin films using ethylenediaminetetraacetic acid disodium salt complexant," *Journal of Solid State Electrochemistry*, vol. 21, no. 9, pp. 2687–2697, 2017.

[50] X. Xue, W. Ji, Z. Mao et al., "Raman investigation of nanosized TiO_2: effect of crystallite size and quantum confinement," *Journal of Physical Chemistry C*, vol. 116, no. 15, pp. 8792–8797, 2012.

[51] A. Virdian, S. Muhammady, M. A. Naradipa, R. Widita, A. Rusydi, and Y. Darma, "Enhancing photon absorption and conductivity of ZnO film by Fe doping: experimental and first-principle perspectives," *Ceramics International*, vol. 46, no. 17, Article ID 27110, 2020.

[52] S. K. Rout, S. Panigrahi, and J. Bera, "Study on electrical properties of Ni-doped $SrTiO_3$ ceramics using impedance spectroscopy," *Bulletin of Materials Science*, vol. 28, no. 3, pp. 275–279, 2005.